https://doi.org/10.5194/egusphere-2023-2797
Preprint. Discussion started: 17 January 2024

The impact of polar warming on global atmospheric circulation and mid-latitude baroclinic waves

Andrei Sukhanovskii[1,3], Andrei Gavrilov[2], Elena Popova[1], and Andrei Vasiliev[1]

[1]Institute of Continuous Media Mechanics UB RAS, 614013, Ac. Korolev Street,1, Perm, Russia
[2]Institute of Thermophysics SB RAS, 630090, Ac. Lavrentieva ave.1, Novosibirsk, Russia
[3]Perm State University, 614068, Bukireva Street.15, Perm, Russia

Correspondence: Andrei Sukhanovskii (san@icmm.ru)

Abstract. The results of experimental and numerical modeling of Arctic warming in a laboratory dishpan configuration are presented. The Arctic warming is reproduced by varying the size of a local cooler in the "atmospheric" regime, in which the flow structure is similar to the general atmospheric circulation. It is shown that a significant variation in cooling power and boundary (slip and non-slip) conditions leads to quantitative changes in the structure and intensity of baroclinic waves. The size of the cooler and boundary conditions applied to its surface play a crucial role in the structure and intensity of circulation at small radii. The laboratory Arctic warming leads to a weakening of a polar cell analog and mean zonal flows. The most important result of this study is a noticeable transformation of the mean temperature field. Namely, the central region and most of the lower layer become warmer, while most of the upper layer and the peripheral (equatorial) part of the lower layer become colder. The nature of this phenomenon is closely related to the changes in radial heat fluxes. Laboratory Arctic warming leads to a significant decrease in the negative heat flux near the bottom, which inevitably leads to an increase in temperature. Our results provide a plausible explanation for Arctic warming amplification.

1 Introduction

Baroclinic waves define the mid-latitude weather, providing meridional transfer of heat and angular momentum (Schneider, 2006). The formation of mid-latitude baroclinic waves is strongly linked to the instability of the axisymmetric zonal flow produced by the Hadley circulation. The study of baroclinic waves in a full statement is an extremely complex problem due to an essentially non-linear nature of the process, which depends on different factors such as rotation, solar heating, and surface topography. The need to reveal robust, intrinsic features of atmospheric baroclinic waves stimulates several laboratory and numerical studies using simplified models (Read et al., 2014). These studies produced very fruitful results to understand the nature and different characteristics of baroclinic waves and showed that the main factors responsible for the formation of baroclinic waves are rotation, cooling and heating. The strong dependence of baroclinic waves on the meridional temperature difference raises questions about possible scenarios of their evolution due to the remarkable warming amplification over the Arctic pole (Arctic amplification), which results in a decrease of the temperature contrast between the pole and the equator (You et al., 2021). Arctic amplification can lead to complex chains of processes that strongly influence large-scale circulation and the likelihood of weather extremes (Overland et al., 2016). The prediction based on numerical calculations suggests that the

https://doi.org/10.5194/egusphere-2023-2797
Preprint. Discussion started: 17 January 2024

Arctic amplification will continue (Wallace et al., 2016). The ice-temperature feedback in the Arctic increases the likelihood of further rapid warming and sea ice loss, and may affect atmospheric circulation in the polar region and mid-latitudes (Screen and Simmonds, 2010). There is some evidence that Arctic amplification increases the meandering of mid-latitude zonal flow and decreases the eastward motion of Rossby waves (Francis and Vavrus, 2015). However, the use of different data, models, approaches, metrics, and interpretations leads to controversial conclusions about the role of Arctic amplification, and joint efforts of the scientific community are needed to reach a generally accepted understanding of the problem (Overland et al., 2016; Stuecker et al., 2018).

Laboratory modeling can help to understand the main tendency of baroclinic wave evolution due to the variations of heating and cooling. There are two main alternative laboratory approaches to the study of baroclinic waves, the so-called dishpan configuration (Fultz et al., 1959) and annulus configuration (Hide, 1953). The main differences are related to the geometry of the fluid layer and the realization of heating and cooling. The dishpan configuration is a cylindrical vessel (usually horizontally extended) with the rim heating at the bottom periphery and cooling in the center, while the annulus configuration is a cylindrical gap between inner and outer cylinders with isothermal vertical walls (inner walls is cold, outer wall is hot). The specifics and comparison of the results for both configurations were described and discussed in (Harlander et al., 2023). The main difference is the tendency of the baroclinic waves to show more intrinsic instability for the dishpan configuration.

Recently, a polar warming scenario has been considered in laboratory experiments carried out in the annulus configuration (Rodda et al., 2022). It was shown that a progressive decrease of the meridional temperature difference slows down the eastward propagation of the jet stream and complicates its structure. Temperature variability decreases relative to the laboratory Arctic warming only at locations representing the polar and mid-latitudes of the Earth, which are influenced by the jet stream. In the subtropical region south of the simulated jet, the trend is reversed. The reduced variability leads to narrower temperature distributions and weaker extreme events, but the frequency of such events increases in the polar and mid-latitudes and decreases towards the subtropics with decreasing meridional temperature difference. The obtained results showed good qualitative agreement with the National Centers for Environmental Prediction (NCEP) reanalysis data. The described scenario of jet variability and frequency of extreme events in a laboratory model is closely related to the baroclinic wave transformation from regular waves with dominant wave numbers to irregular regimes with a wide range of excited wave numbers due to a substantial decrease in the applied temperature difference and thermal Rossby number. It is unclear whether this scenario is a robust and intrinsic feature of baroclinic waves in rotating tanks with horizontal temperature difference or a specific feature of a particular laboratory realization in the annulus configuration. In order to resolve this issue, we conducted a series of experiments and numerical simulations for the Arctic warming scenario in the dishpan configuration (Sukhanovskii et al., 2023; Vasiliev et al., 2023). The combined laboratory and numerical approach allow to reveal qualitative and quantitative aspects of the complex system under consideration.

The structure of the paper is as follows. The statement of the problem and governing parameters are given in section 2, the experimental set-up and mathematical model are described in section 3. The main results, including description of the flow structure (subsection 4.1) and heat transfer analysis (subsection 4.2) are presented in section 4. A summary and conclusions are given in section 5.

https://doi.org/10.5194/egusphere-2023-2797
Preprint. Discussion started: 17 January 2024

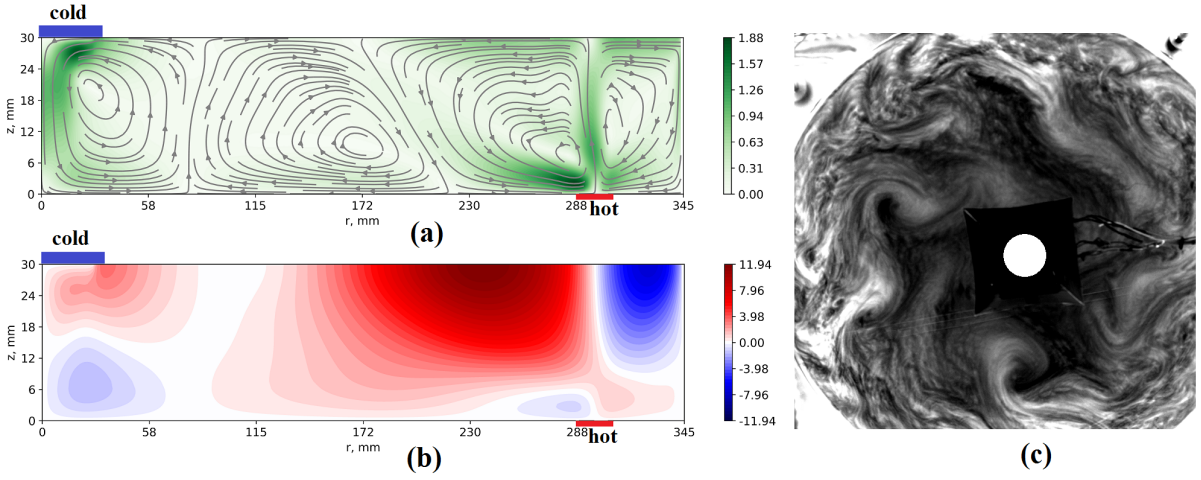

Figure 1. The typical structure of the laboratory analog of atmospheric circulation (in the rotating frame). (a) Mean meridional circulation, (b) Mean azimuthal flows, color bars show the velocity magnitude in $\mathrm{mm/s}$ (numerical simulation), (c) Instantaneous image of the flow structure (visualization by aluminum powder, view from above). (Colour online)

2 Statement of the problem and governing parameters

In the present study we consider a shallow rotating cylindrical layer of fluid with a localized heater at the bottom in the periphery and a localized cooler in the central part of the upper boundary. The rim heater mimics the equatorial heating and the disc cooler mimics the north pole cooling. The rim heater is intentionally shifted from the sidewall to reduce the influence of the non-slip vertical boundaries. Boundary conditions of the second type (constant heat flux) are chosen because they are more realistic for the atmosphere. This configuration allows one to realize a variety of flow regimes from axisymmetric to highly irregular (Sukhanovskii et al., 2023; Vasiliev et al., 2023). Motivated by the problem of Arctic warming we examine how central cooling affects the structure and characteristics of the flow, which is similar to the typical atmospheric circulation. The mean meridional circulation (Fig. 1a) includes analogs of the polar cell at small radii, the weak Ferrel cell (which is seen only after averaging over azimuthal coordinate and time) at middle radii and the Hadley cell at the periphery. The shift of the heater from the sidewall leads to the formation of an additional cell to the right of the Hadley cell analog. This fourth cell provides anticyclonic circulation near the sidewall, which resembles easterly winds in the lower latitudes (Fig. 1b). In the upper layer, the analogs of the polar and Hadley cells transport the fluid with relatively large values of angular momentum to the smaller radii, providing formation of pronounced cyclonic zonal flows. A weak cell in the middle radii is the result of a train of baroclinic waves (Fig. 1c) that efficiently transport heat from the analog of the Hadley cell to the polar cell. To model Arctic warming, we vary the size and power of the central cooler for a fixed heat flux at the periphery. There are many issues associated with the Arctic amplification problem, but in the present study we limited ourselves to considering changes in the mean flow structure, mean heat transport, and baroclinic wave characteristics.

https://doi.org/10.5194/egusphere-2023-2797
Preprint. Discussion started: 17 January 2024

As non-dimensional governing parameters, following (Scolan and Read, 2017), we use the thermal Rossby number Ro_T, the Taylor number Ta, and the Ekman number E:

$$Ro_T = \frac{g\alpha h \Delta T}{\Omega^2 R^2}, \tag{1}$$

$$Ta = \frac{4\Omega^2 R^5}{h\nu^2}, \tag{2}$$

$$E = \frac{\nu}{\Omega h^2}, \tag{3}$$

where g is the gravitational acceleration, α is the thermal expansion coefficient, ΔT is the temperature difference between heater and cooler, Ω is a rotation rate, R is the radius of the layer, and ν is the kinematic viscosity.

Several remarks should be made regarding the thermal Rossby number. It is a key parameter used in the study of a rotating cylinder gap filled with a fluid and isothermal sidewalls. Here we consider a rotating shallow cylindrical layer with non-uniform heating and cooling at horizontal boundaries. Moreover, instead of a constant temperature (first type boundary conditions), a constant heat flux is applied (second type boundary conditions). Therefore, we provide values of Ro_T for comparison with the results of other studies, but this should be done with caution.

3 Methods

3.1 Experiment

A detailed description of the laboratory model of general atmosphere circulation is given in (Sukhanovskii et al., 2023; Vasiliev et al., 2023). The experimental model is a rectangular tank of a square cross-section with a side $L = 700$ mm, and height $H = 200$ mm (figure 2). The sidewall and bottom are made of Plexiglas with a thickness 20 mm. For the realization of the cylindrical layer the Plexiglas cylinder with a 3 mm wall and diameter $D = 690$ mm is inserted into the tank. The heater is a 25 mm wide circular strip of thin copper foil heated by an electric current. The distance from the cylindrical sidewall to the outer border of the heater is 40 mm. The heating power is controlled and kept constant during the experiment. The room temperature is kept constant by an air-conditioning system, and the cooling of the fluid is provided by the heat exchange with the surrounding air on the free surface, the central cooling system and some heat losses through the sidewall. The cooling system includes a thick (10 mm) copper disc with diameter $d = 56$ mm partially inserted into the upper layer of the fluid (about 2 mm). The upper surface of the copper disc is cooled by a thermoelectric (Peltier) cooler. To remove heat from the hot side of the thermoelectric cooler a radiator with a forced air circulation is used. For minimization of the impact of the air circulation, the cooling system is surrounded by an additional open box. Note that the size of the cooler, which is in direct contact with a fluid, is substantially less than the visible part of the cooling system (the white circle in the center of a figure 1c). The temperature of the cooler was measured by a copper–constantan thermocouple installed into the copper disc.

The experimental model is placed on a rotating horizontal table. The rotating table provides a uniform rotation in the angular velocity range $0.02 \leq \Omega \leq 0.30$ rad s^{-1} (with accuracy of ± 0.001 rad s^{-1}). The silicon oil PMS-5 (see Table 1) is used as the working fluid. In all the experiments presented, the depth of the fluid layer h was 30 mm and the surface of the fluid was open.

https://doi.org/10.5194/egusphere-2023-2797
Preprint. Discussion started: 17 January 2024

Fluid properties	Symbol	Value	Units
Density	ρ	911	kg m^{-3}
Kinematic viscosity	ν	5.2×10^{-6}	m^2 s^{-1}
Thermal diffusivity	κ	8.3×10^{-8}	m^2 s^{-1}
Thermal expansion coefficient	α	9×10^{-4}	K^{-1}
Prandtl number	$Pr = \nu\,\kappa^{-1}$	62.7	
Experimental set-up			
Layer radius	R	345	mm
Layer depth	h	30	mm
Heater width	l	25	mm
Heater radius	r_h	293	mm
Cooler radius	r_c	28	mm
Heating power	P_h	123	Wt
Cooling power	P_c	≈ 3	Wt

Table 1. The main fluid properties and parameters of the experimental model.

The temperature inside the fluid layer was measured at mid-height ($z = 15$ mm) and $R = 180$ mm by the copper–constantan thermocouple and used for the estimation of the mean temperature of the fluid. The main fluid properties and parameters of the experimental set-up are provided in Table 1. The direction of rotation in all experiments was clockwise.

Aluminum flakes are used to visualize the flow structure in the upper layer. The illumination of the tracers is provided by LED (light-emitting diode) strip placed on the perimeter of the experimental model above the fluid layer. The aluminum flakes are oriented along the flow, so they are bright when the flow is horizontal and dark when vertical motions are dominant. The recording was provided by 4 Mpx CCD camera Bobcat 2020 with 1 fps.

It should be noted that the cooler in the experiment is relatively small. This was done deliberately to minimize the loss of angular momentum due to friction at the solid boundary (Evgrafova and Sukhanovskii, 2022) and intensification of vertical circulation by Ekman pumping. The cooler induces intensive descending flow in the central area, but the substantial difference in the heating and cooling areas leads to a drastic difference between cooling and heating power. This means that most of the cooling is provided by the heat exchange between the fluid and the air on the open surface.

3.2 Numerical simulation

The experiments carried out to study the flow structure at the upper level yielded valuable information, but they are not sufficient to understand all aspects of a complex system. An effective way to solve this problem is numerical simulation using a digital "twin" of the laboratory model. This has already been demonstrated with the mathematical model implemented by

https://doi.org/10.5194/egusphere-2023-2797
Preprint. Discussion started: 17 January 2024

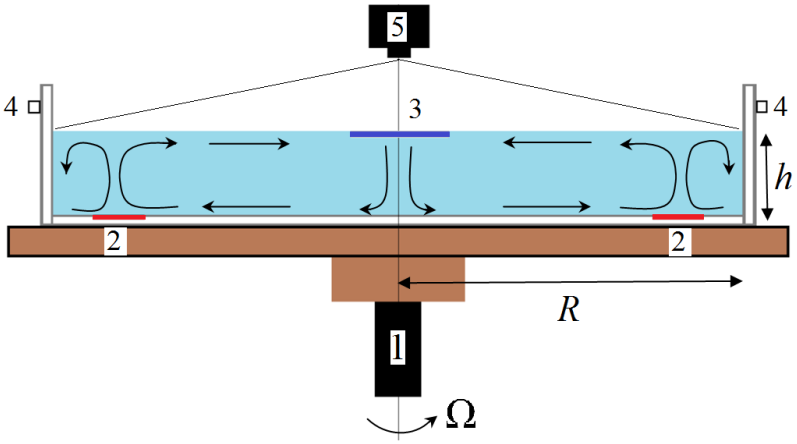

Figure 2. Scheme of the laboratory model, 1 - rotating table, 2 - rim heater, 3 - cooler, 4 - LED illumination, 5 - CCD camera. (Colour online)

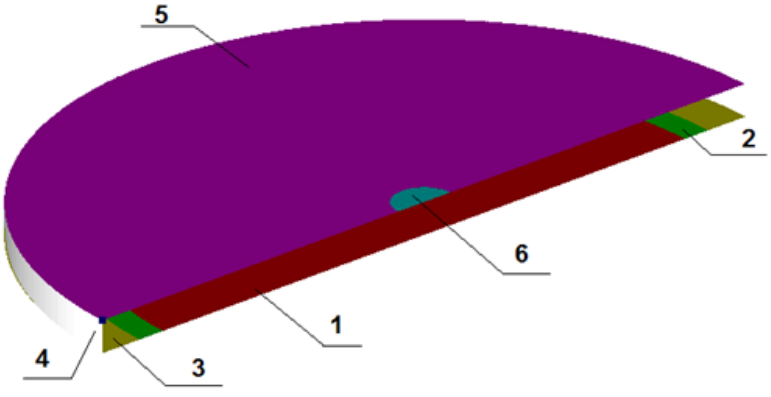

Figure 3. Geometry and boundaries of the computational domain. 1,3,4 - adiabatic walls, 2 - rim heater, 5 - free surface with constant heat flux, 6 - cooler. (Colour online)

the freely distributed computational fluid dynamics package OpenFOAM v2106 (Vasiliev et al., 2023). In the present study, the mathematical model of the laboratory system implemented by the in-house CFD code σFlow was used for numerical simulations.

The scheme of the numerical model is shown in Fig. 3. The model consists of a rotating fluid layer in the cylindrical cavity with local cooling and heating. Most of the characteristics of the numerical model are similar to the laboratory model, but some differences should be mentioned. In the experiment, cooling at the top surface is provided by ambient air circulation and is not uniform. In numerical simulations, we apply a constant heat flux at the free fluid surface. In order to check the influence of the solid boundary of the cooler, we use both non-slip and slip conditions for the surface of the cooler. Another important issue is the size of the cooler and its performance. To address this issue, we perform a series of numerical simulations with a

https://doi.org/10.5194/egusphere-2023-2797
Preprint. Discussion started: 17 January 2024

larger cooler (Table 3). The unsteady flow of an incompressible fluid is modeled in the Boussinesq approximation (in a rotating reference frame). The equations in a rotating reference frame are formulated in terms of the absolute velocity components.

Boundary conditions The boundary conditions are chosen to mimic the experimental apparatus. Non-slip conditions are imposed on all solid walls, including the cooler surface. A slip condition is imposed on the free boundary. Constant uniform heat fluxes are applied to the heater, cooler, and free surface, determined by the given net heat power of the corresponding surface. The heat power of the free surface is equal to the difference between the heat powers of the heater and the cooler. The other surfaces are adiabatic. As an initial approximation for the velocity, the condition of solid body rotation at a given rotational speed is used. The initial uniform temperature of the fluid is equal to the reference temperature T_0 = 20°C.

Discretization The unstructured computational grid is constructed from several blocks with a structured hexagonal mesh. The mesh blocks distinguish the heater and cooler regions. A detailed description is given in the section on computational verification.

The time step remained constant during the calculation and was set to 0.05 s. For the base mode with a rotation period T = 27 s, the maximum Courant number (CFL) calculated using the relative velocity does not exceed unity, and the volume average CFL = 0.085. The mean characteristics are obtained by averaging over time and along a uniform azimuthal direction after reaching the statistical steady state regime, which takes about 2000 c. The averaging time is at least 7600 s.

The numerical algorithm implemented in the CFD code σFlow is based on the finite volume method for the unstructured mesh. The highlights of the algorithm are briefly listed below. For the spatial discretization, central differencing is used for the diffusion terms, and the convective terms of the momentum equation are approximated by a central second order difference scheme. A version of the Total Variation Diminish (TVD) scheme is used for the convective term in the heat energy transport equation. The numerical algorithm is based on a SIMPLE-like pressure correction procedure and a collocated grid array with Rhie-Chow interpolation. The unconditionally stable second order Crank-Nicolson method is used for the time integration. Both viscous and convective terms of the equation of motion are implicitly approximated. The system of linear algebraic equations for the pressure correction equation is solved using an algebraic multigrid solver.

Verification Verification of the simulation was performed by comparing the numerical results obtained on three different meshes. Verification calculations were performed for the basic mode with a rotation period $T = 27$ s, and heat power $\mathrm{Q_h}$ = 123 Wt (heater), $\mathrm{Q_c}$ = -3 Wt (cooler), $\mathrm{Q_{fs}}$ = -120 Wt (free surface). Approximately the basic grid has the following spatial discretization: N_r = 192 nodes in radial direction with clustering of nodes to the heater and cooler, N_ϕ = 260 nodes in tangential direction and N_z = 40 nodes in vertical direction with clustering factor to the boundaries 1.05. The total number of control volumes is $N_r \times N_\phi \times N_z$ = 2.0 million cells. The fine mesh has the following discretization: N_r = 375, N_ϕ = 480, N_z = 60, total number of control volumes 10 million. The coarse grid discretization is as follows: N_r = 90, N_ϕ = 100, N_z = 30, total number of control volumes 0.285 million cells.

Using the numerical solution on three grids we can perform a procedure for the estimation of grid convergence and discretization error. The discretization error is calculated by the algorithm described in (Celik et al., 2008). Table 2 presents the results of the grid convergence analysis for the radial distributions of temperature difference $T - T_0$, turbulent kinetic energy k, relative tangential velocity V_ϕ and turbulent radial heat flux q_t. The obtained apparent order of spatial approximation p is found

https://doi.org/10.5194/egusphere-2023-2797
Preprint. Discussion started: 17 January 2024

Parameter	|value|	p	GCI(fine), %	GCI(base), %	GCI(coarse), %
$T - T_0$	4.146 K	1.288	1.2	2.4	5.4
k	10^{-5} m^2 s^{-2}	1.985	1.7	5.1	18
V_ϕ	0.00789 m/s	1.718	1.7	4.3	12.8
q_t	0.00087 mK/s	1.991	1.2	3.5	12.5

Table 2. Estimation of discretization error.

to be close to the formal second order of accuracy, with the exception for the temperature field. This agreement is an indication of the grids being in the asymptotic range. The difference between the apparent and formal orders for the temperature field is most likely due to the upwind TVD scheme for convective terms. The values of the grid convergence indices are normalized to the values indicated as |value| in the Table 2. The fine-grid convergence index GCI, determined by comparing the results obtained for the detailed and basic grids, does not exceed 5%. The presented data confirm that the numerical accuracy of the base mesh is within acceptable limits for CFD simulation.

4 Results

4.1 Flow structure

Earlier in (Sukhanovskii et al., 2023) it was shown that the atmospheric regime, in which the mean flow and baroclinic waves are similar to those in the real atmosphere, i.e. strongly non-stationary waves with main modes $m = 2-8$ (see mode decomposition analysis in (Lembo et al., 2019, 2022)), can be realized only in a short interval of the main parameters. We have chosen this regime to study Arctic warming using laboratory and numerical modeling. To examine the role of localized cooling, we vary the size of the cooler and consider three cases: a large cooler ($r_c = 46$ mm, only in the numerical simulation), a small cooler ($r_c = 28$ mm) and uniform cooling at the free surface, without a local cooler. The heat flux for the large cooler was the same as for the small one, so the power of the cooler increased proportionally to its area from 3 Wt to 8 Wt. The net cooling power, including the free surface, is the same for all cases considered – 123 Wt. In order to better understand the role of Ekman pumping (due to the non-slip condition in the cooling area), we perform numerical simulations in the "atmospheric" regime for the central cooling of the large size ($r_c = 46$ mm) with non-slip boundary conditions. The main parameters of the experiments and numerical simulations are presented in Table 3.

Examples of the flow structure for the atmospheric regime with and without central cooling in experiments (case 3 and 4,Table 3) are shown in figure 4. For both cases the baroclinic waves in middle radii are not regular and are characterized by strong temporal and spatial variations. The difference in the flow structure between two configurations is not obvious. Typical flow structures for all four cases, considered in numerical simulations are shown in figure 5. Surprisingly, a significant increase in size and cooling power, and a change from non-slip to slip boundary conditions (figure 5a,b), does not lead to a noticeable

https://doi.org/10.5194/egusphere-2023-2797
Preprint. Discussion started: 17 January 2024

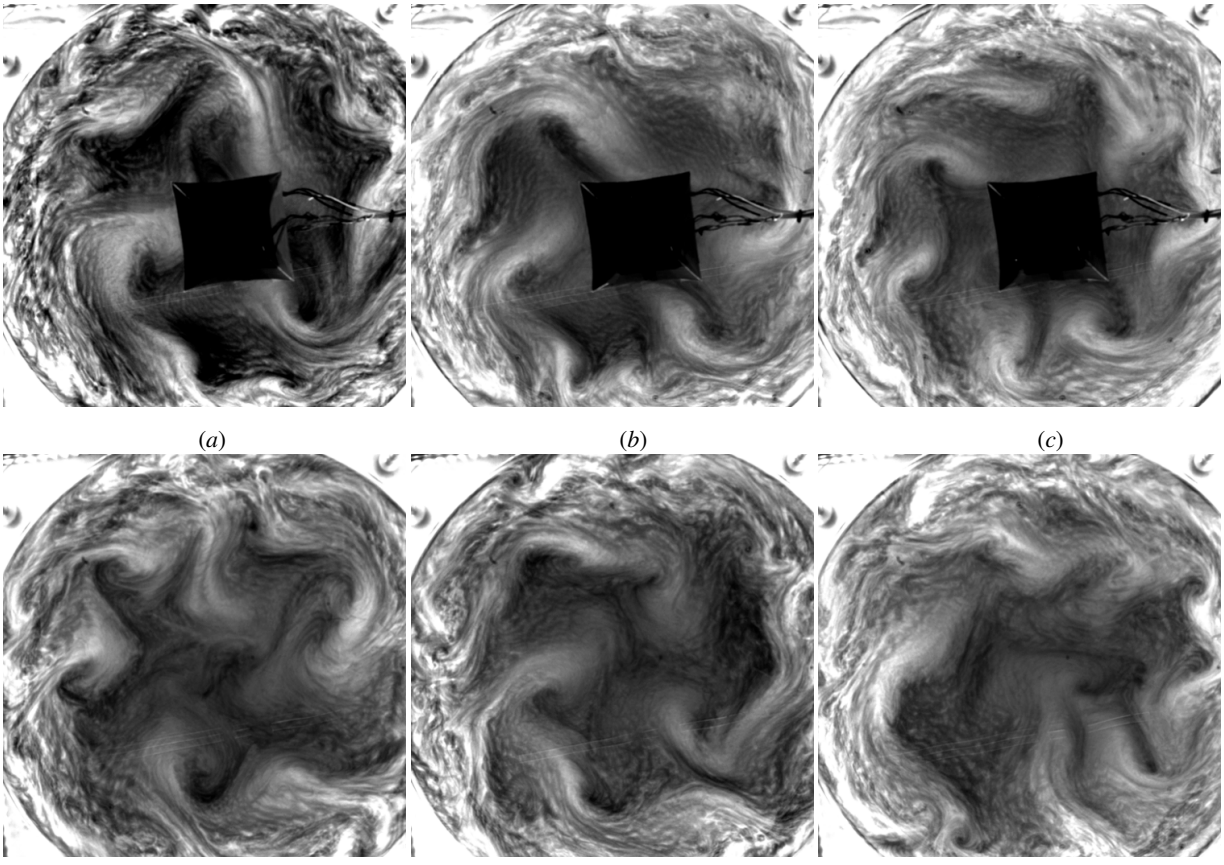

Figure 4. Examples of the flow structure in the atmospheric regime (cases 3 and 4). Upper panel (a-c) with cooler, lower panel (d-f) without central cooler. Experiment.(Colour online)

Case	Ω, rad s^{-1}	Q_c	r_c, mm	ΔT	Ro_T	Ta	E	BC_{cooler}	$real.$
1	0.37	8	46	20.3	0.34	3.6×10^9	0.015	slip	num
2	0.37	8	46	24.3	0.41	3.6×10^9	0.015	non-slip	num
3	0.37	3	28	24.1	0.4	3.6×10^9	0.015	non-slip	exp/num
4	0.37	-	-	17.1	0.29	3.6×10^9	0.015	no cooler	exp/num

Table 3. Main parameters of experiments and numerical simulations

https://doi.org/10.5194/egusphere-2023-2797
Preprint. Discussion started: 17 January 2024

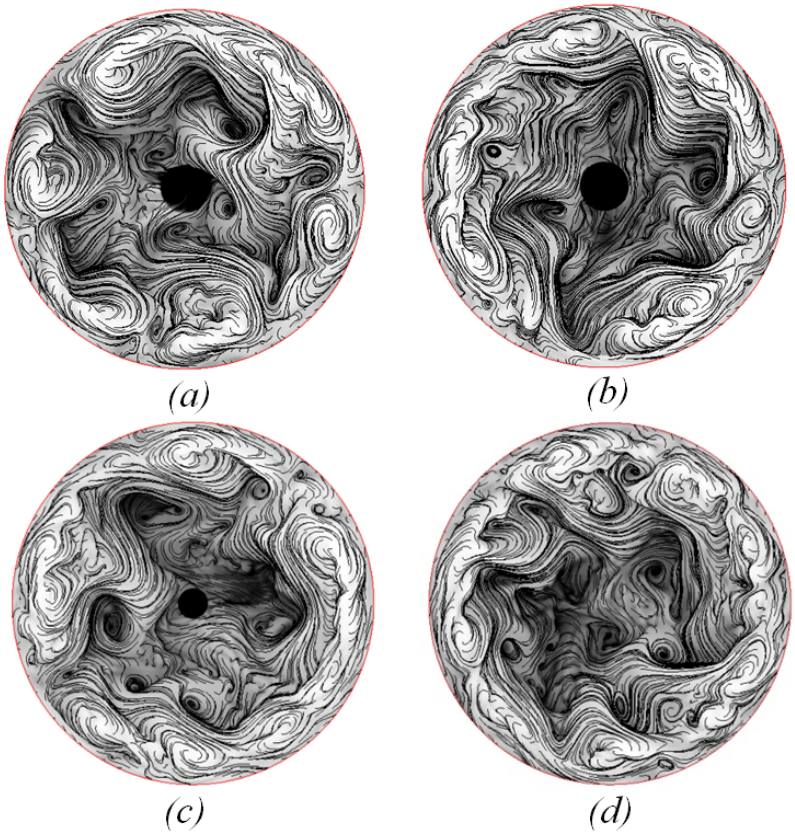

Figure 5. Typical flow structure at the top layer for different configurations, a – large slip cooler, b – large no-slip cooler, c – small no-slip cooler, d – no cooler. Numerical simulation.(Colour online)

change in the flow structure. In general, the instantaneous flows observed in the atmospheric regime are rather irregular and similar for all configurations under study.

Qualitative observations of the flow structure in the upper layer provide only partial information about the flow. Using numerical modeling, we can reconstruct the flow structure in the vertical cross section and show quantitative differences between different configurations. The mean flows in a vertical cross section (meridional circulation) for different configurations are shown in figure 6. There is a significant difference in the flow structure between two configurations with the large cooler but under different boundary conditions (figure 6a,b). The cooler with non-slip boundary condition has a viscous boundary layer (Ekman layer), which leads to an additional circulation, known as the Ekman pumping. Analysis of the results obtained indicates that the Ekman pumping provides an intensive downward flow near the axis of rotation, which is crucial for the structure of the laboratory polar cell. If we turn off the Ekman pumping using slip boundary conditions, then the polar cell analog becomes substantially weaker and changes its shape. The polar cell moves up and closer to the middle radii. A decrease in the size of the non-slip cooler results in a decrease of the size of the polar cell but the overall structure remains unchanged.

https://doi.org/10.5194/egusphere-2023-2797
Preprint. Discussion started: 17 January 2024

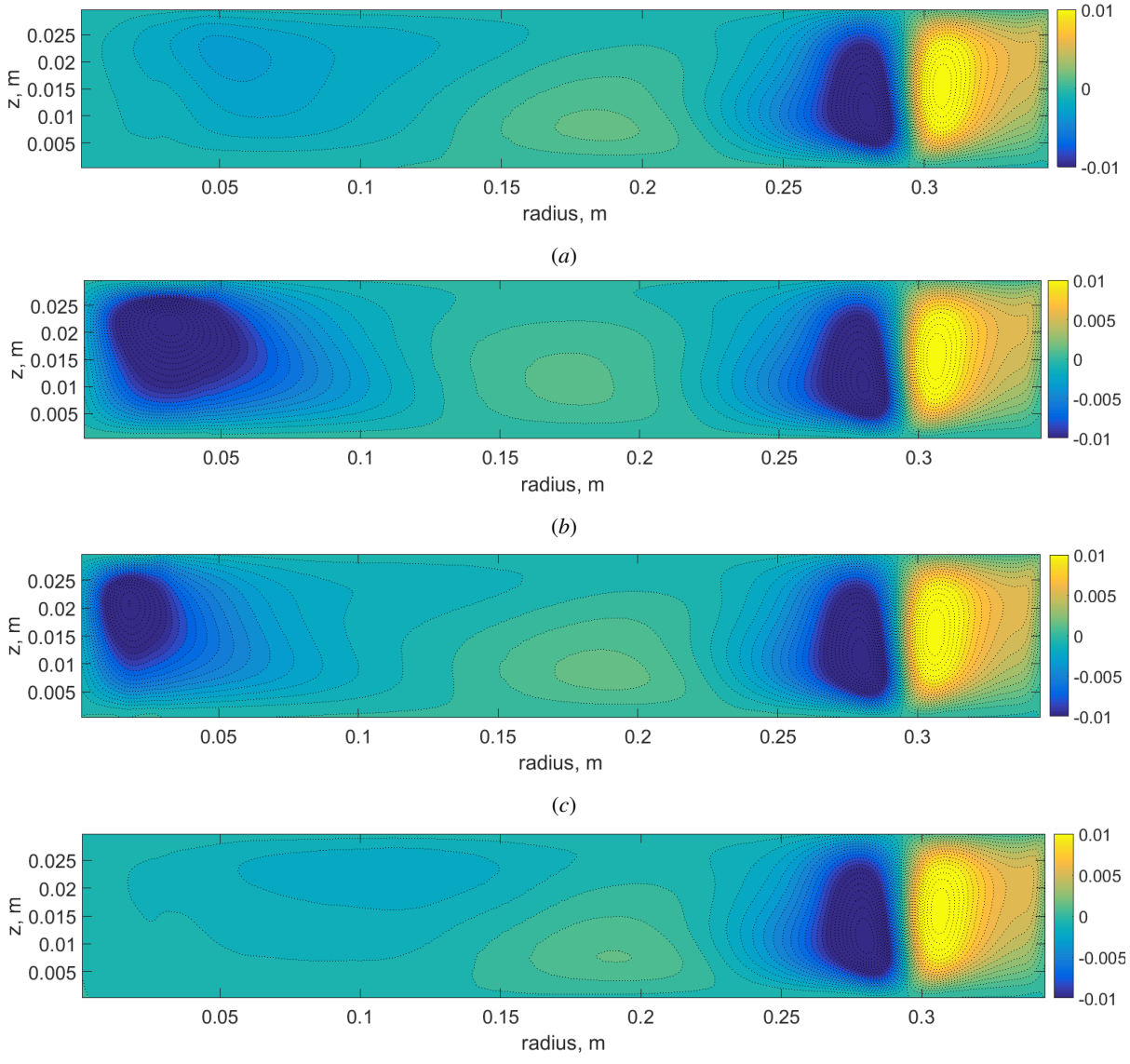

Figure 6. Mean meridional circulation (stream function) for different cases, a – case 1 (large slip cooler), b – case 2 (large non-slip cooler) , c – case 3 (small non-slip cooler), d – case 4 (no cooler).Numerical simulation. (Colour online)

205 If we consider the case without cooler (uniform heat flux at the free surface), then the polar cell structure is similar to the case with the large slip cooler but the polar cell analog becomes even weaker, shifts closer to middle radii and is located in the upper layer. Based on the results, we can conclude that the size and boundary conditions at the cooler surface play a key role for the structure and intensity of the polar cell analog.

https://doi.org/10.5194/egusphere-2023-2797
Preprint. Discussion started: 17 January 2024

Another important issue related to Arctic warming is the change in the azimuthal velocity distribution. Meridional cells transfer the angular momentum and provide the formation of the differential rotation (zonal flows). We can expect that the transformation of the polar cell analog achieved by varying the size and intensity of local cooling would lead to the change of the zonal flow structure and intensity. Figure 7 shows the mean azimuthal velocity fields (averaged over time and azimuthal coordinate) for different cases. In fact, the main changes are observed in the central region due to a significant change in the structure of the central meridional cell. Of particular interest are cases 1 and 4 (large slip cooler and no cooler), because for these cases the Ekman pumping is excluded. A change in the zonal flow (azimuthal velocity) between these two cases is shown in figure 7d. The transition from non-uniform cooling (local intensive cooling near the central axis and uniform cooling on the rest of the free surface) to uniform cooling on the whole surface results in a weakening of the zonal flows.

The next question concerns the influence of localized cooling on the characteristics of baroclinic waves that provide the radial transport of heat and angular momentum. To illustrate the intensity and location of baroclinic waves, we present distributions of the mean energy of radial velocity fluctuations $E_{bw} = \langle u_r^2 \rangle_{\phi,t}$ in a vertical cross section (Figure 8). In all cases considered (large cooler with slip and non-slip conditions, small non-slip cooler, no cooler) the location of baroclinic waves and their energy distribution are similar. The baroclinic waves are formed in the upper part of the layer with maximum intensity at $r \approx 0.22$m. It is evident that the cooler with non-slip boundary conditions efficiently suppresses radial velocity pulsations. The profiles of E_{bw} at the top of the layer are shown in figure 9a. In the case of large slip cooler there is a second maximum of E_{bw}, non-slip cooler results in a sharp decrease of E_{bw} and in the case without localized cooler there is a monotonic decrease of E_{bw}. The baroclinic waves in the atmospheric regime are the superposition of different wave modes in the azimuthal direction, and their energy can be estimated by Fourier decomposition (see e.g. (Sukhanovskii et al., 2023)). The energy of main baroclinic modes at $r = 0.22$m is shown in figure 9b. As in the real atmosphere, modes $m = 4 - 8$ contain most of the baroclinic wave energy. The change of the boundary condition (slip, non-slip), the area and the local cooling power give noticeable deviations of the energy of different modes up to 25%.

4.2 Heat transfer and variation of the mean vertical temperature field

The main function of the large-scale meridional circulation and mid-latitude baroclinic waves is to transfer heat from the equator to the polar region. Figure 10a shows the distribution of the total mean radial heat flux (averaged over azimuthal coordinate, height and time) along the radius. In the quasi-stationary state, the total heat flux is directed toward the center (polar region) and decreases monotonically due to cooling at the free surface and by the local cooler. The total heat flux can be divided into two parts, mean and pulsating (figure 10b), provided by the mean circulation and mean temperature distribution, and pulsations of velocity and temperature:

$$q_{full}(r) = 2\pi r(\langle U_r T \rangle_{\phi,h} + \langle u_r T' \rangle_{\phi,h,t}) \tag{4}$$

, where U_r,T are the mean (over time) radial velocity and temperature, and u_r,T' are the pulsations of radial velocity and temperature.

https://doi.org/10.5194/egusphere-2023-2797
Preprint. Discussion started: 17 January 2024

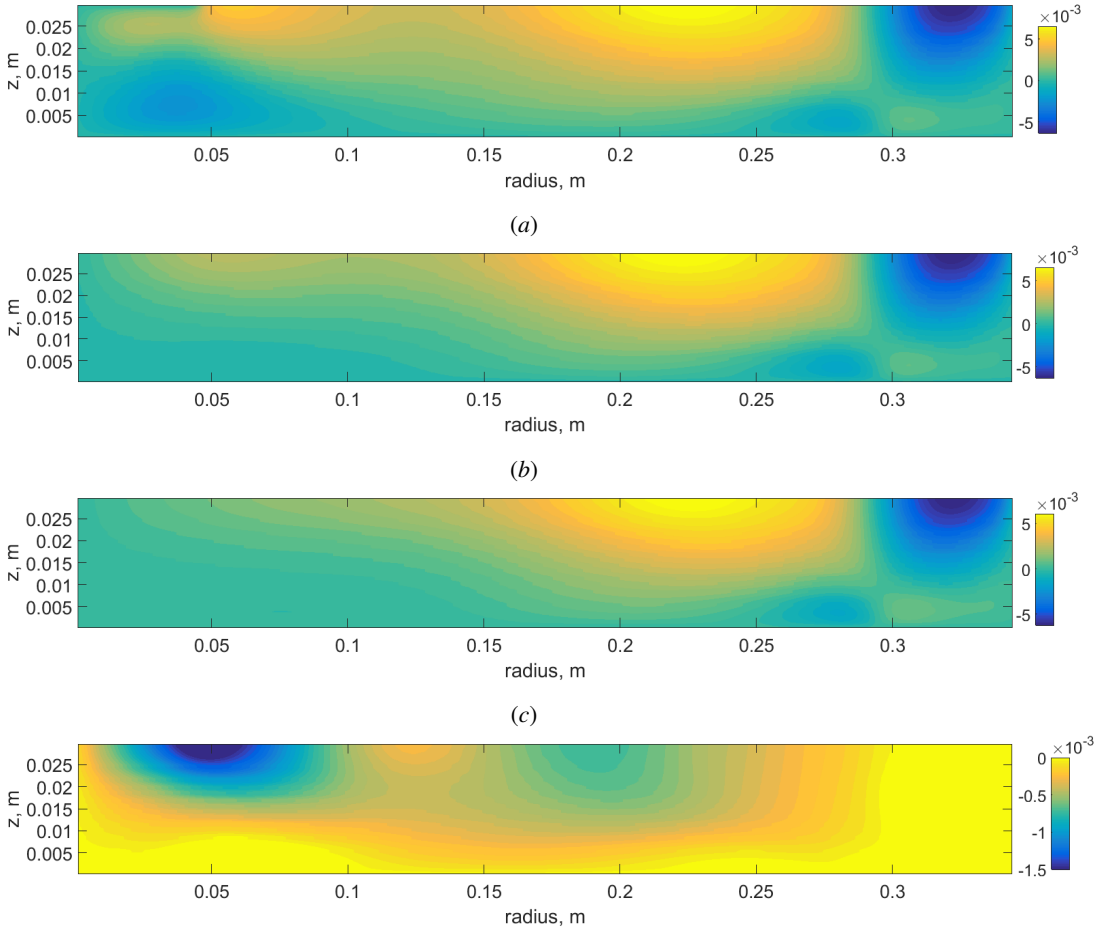

Figure 7. (a-c) – mean vertical fields of relative azimuthal velocity (in a rotating frame). (a) – large cooler, non-slip condition (V_{lc}), (b) – large cooler slip condition (V_{lcs}), (c) – without cooler V_{nc}; (d) – change of azimuthal velocity for cases (b) and (c) $\Delta V = V_{nc} - V_{lcs}$. Atmospheric regime, velocity in m/s. Numerical simulation.(Colour online)

https://doi.org/10.5194/egusphere-2023-2797
Preprint. Discussion started: 17 January 2024

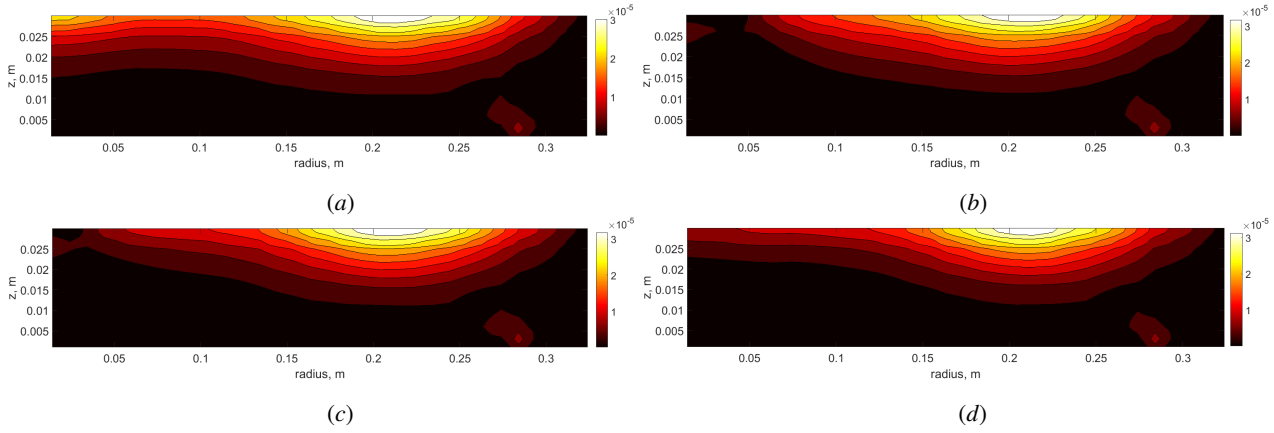

Figure 8. Vertical field of energy of radial velocity fluctuations, (a) – large cooler, slip condition, (b) – large cooler, non-slip condition, (c) – small cooler, non-slip condition, (d) – no cooler. Numerical simulation. (Colour online)

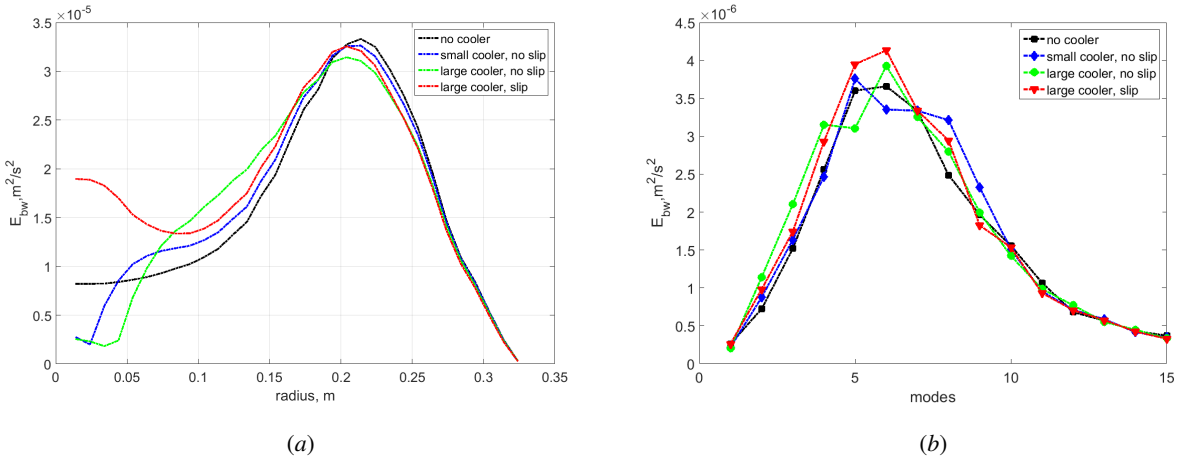

Figure 9. (a) – profiles of energy of radial velocity fluctuations at the top of the layer, (b) – energy of different modes of radial velocity fluctuations at the top of the layer. Different cooling configurations in the atmospheric regime.(Colour online)

https://doi.org/10.5194/egusphere-2023-2797
Preprint. Discussion started: 17 January 2024

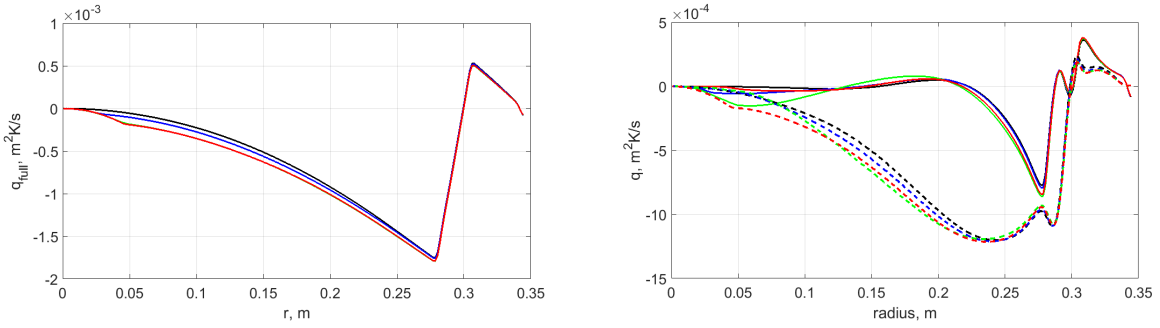

(*a*) (*b*)

Figure 10. (a) – total radial heat flux (integrated over the azimuthal coordinate), averaged over time and height, black line – without cooling, blue line – small cooler, green line – large cooler, non-slip condition, red line – large cooler, slip condition; (b) – mean (solid lines) and pulsating (dotted lines) parts of the total heat flux. Atmospheric regime. Numerical simulation. (Colour online)

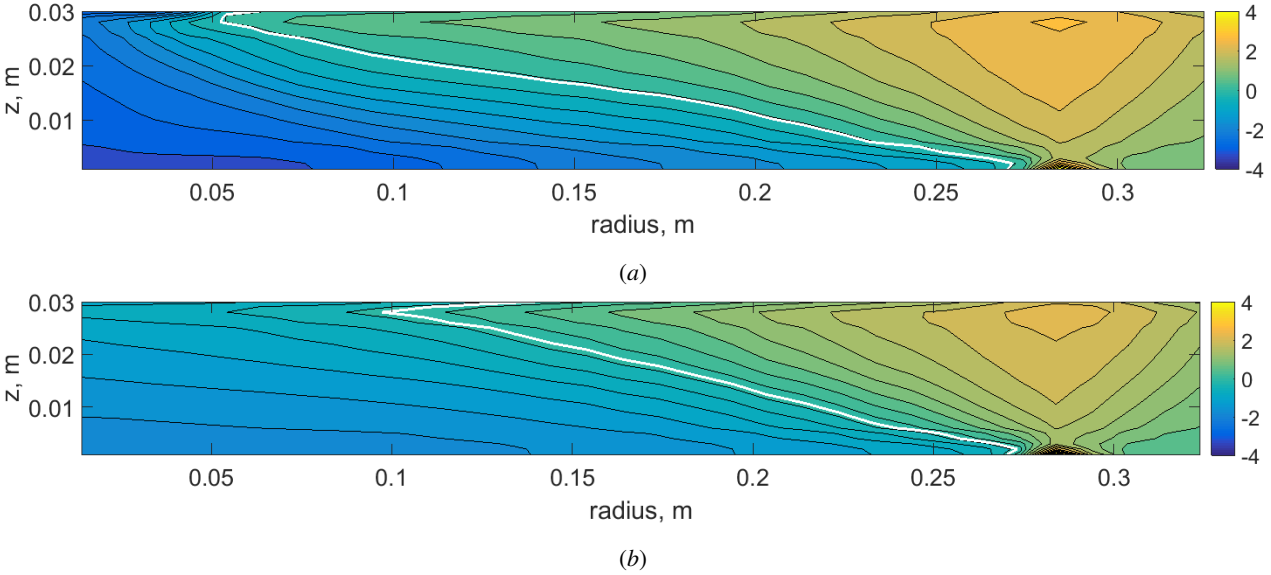

(*a*)

(*b*)

Figure 11. Mean vertical temperature fields (averaged over azimuthal coordinate and time). (a) – with large cooler and non-slip condition (T_{lc}), (b) – without cooler (T_{nc}). The mean temperature of the fluid ($T_0 = 293$ K) is subtracted. The solid white line shows zero isotherm. Atmospheric regime. Numerical simulation. (Colour online)

https://doi.org/10.5194/egusphere-2023-2797
Preprint. Discussion started: 17 January 2024

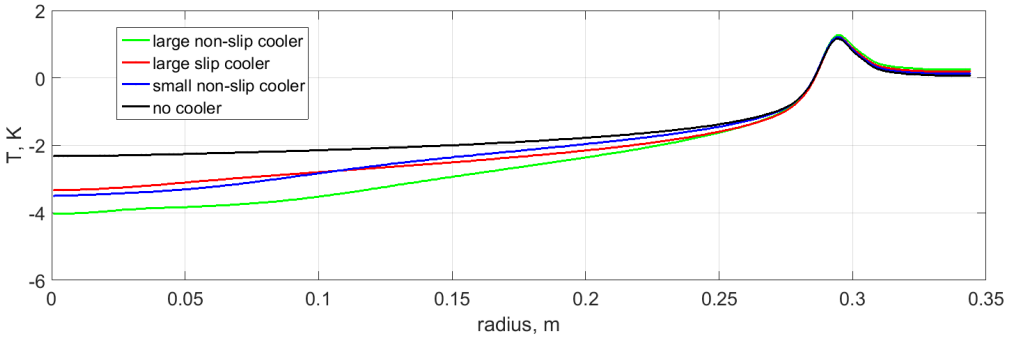

Figure 12. Mean temperature profiles in the lower layer ($z = 0.002$ m), green line – large cooler, non-slip condition, red line – large cooler, slip condition, blue line – small cooler, black line – without cooling. The mean temperature of the fluid ($T_0 = 293$ K) is subtracted. The solid white line shows zero isotherm. Atmospheric regime. Numerical simulation. (Colour online)

It is obvious that the pulsating part of the heat flux plays the key role in the heat transfer towards the polar region. Only in the case of a large non-slip cooler the mean heat flux (solid green line in figure 10b) is dominant in the polar region due to the effective suppression of the wave motion. The profiles of the mean (over height) heat flux for all cases are quite similar, because the variations of the boundary conditions are relatively weak, except in the region of the localized cooler. The heat flux in the heating region is strictly the same, and the variations of the heat flux at the upper surface are only noticeable in the localized cooler zone. However, the distribution of the heat flux (which is mostly convective) along the vertical coordinate depends strongly on the flow structure. According to this, we can expect substantial spatial variations of the heat flux and, as a consequence, of the mean temperature distribution change, due to the remarkable transformation of the polar cell, which we described earlier. To check this assumption, we compare the mean vertical temperature fields for substantially different polar cell structures, namely, for the cases with a large non-slip cooler and without a cooler (figure 11). In fact, there is a noticeable change in the temperature distribution, mainly in the central region and in the lower layer. For practical applications (e.g. weather forecasting) the surface temperature is one of the most important parameters. The mean temperature profiles near the bottom, are shown in Figure 12. The main result is that the transition from non-uniform to uniform cooling conditions leads to an increase in temperature near the bottom, up to the heating region. Note that for all cases considered, the mean temperature of the fluid ($T_0 = 293$ K) and the total heating and cooling power are the same. The only difference is the distribution of the cooling flux on the top surface. It is either non-uniform in the cases with a localized cooler or uniform in the case without a localized cooler. Noticeable changes in the temperature distribution can be better seen by plotting the temperature difference for different cases (figure 13)a,b. The removal of the local cooler leads to a significant transformation of the mean temperature field. The central region and most of the lower layer become warmer, while most of the upper layer and the peripheral (equatorial) part of the lower layer become colder. For the non-slip cooler, the temperature trends are stronger due to Ekman pumping, but for the slip cooler, which is a better approximation of real atmospheric conditions, the effect is also substantial. To compare the numerical results with experimental data, temperature measurements were made by an

https://doi.org/10.5194/egusphere-2023-2797
Preprint. Discussion started: 17 January 2024

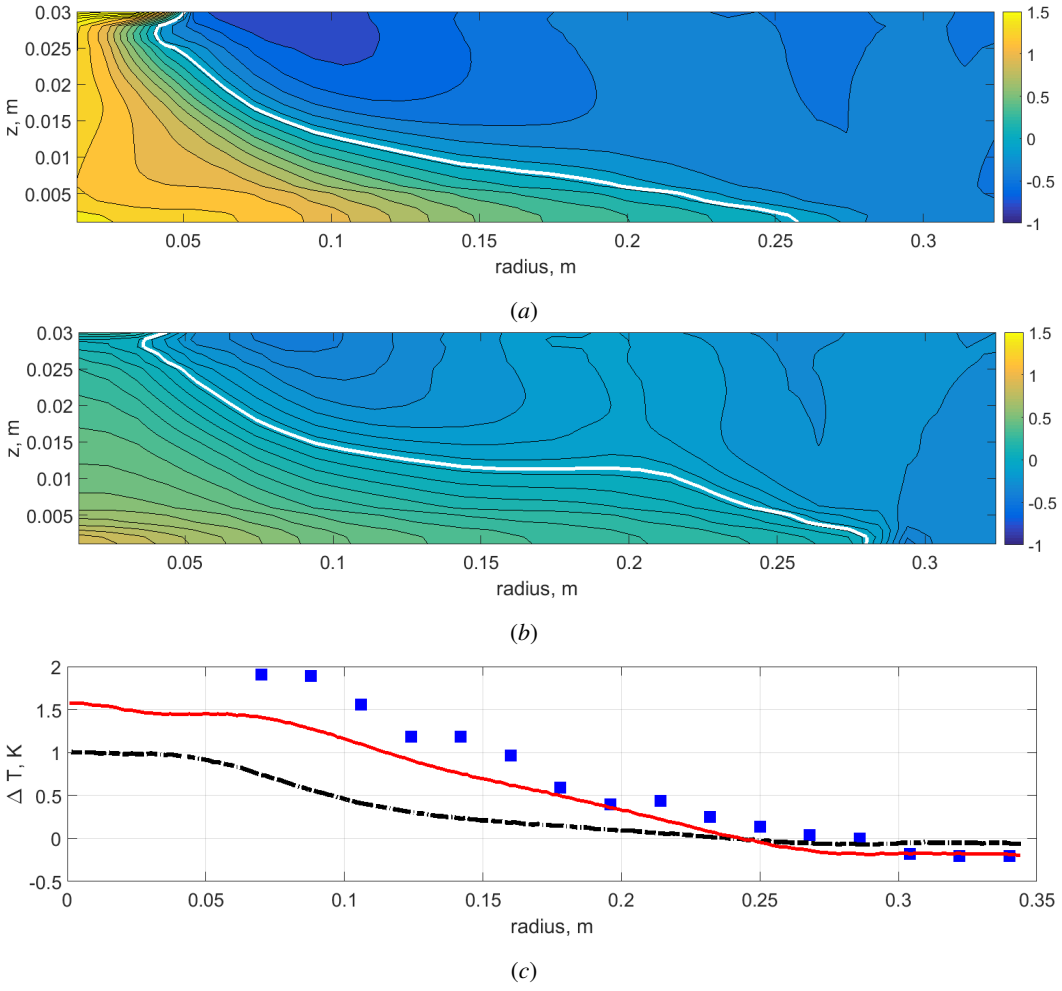

Figure 13. (a) – temperature difference $\Delta T_1 = T_{nc} - T_{lc}$, where T_{nc} – mean vertical temperature field without cooler and T_{lc} – with large non-slip cooler (numerical simulation); (b) – temperature difference $\Delta T_2 = T_{nc} - T_{lcs}$, where T_{lcs} – mean vertical temperature field with large slip cooler (numerical simulation); (c) – profiles of temperature difference at $z = 5$ mm, black dotted line – $\Delta T_3 = T_{nc} - T_c$, where T_c – mean vertical temperature field with a small non-slip cooler, red solid line – ΔT_1, squares – ΔT_3, experimental measurements by array of thermocouples. Atmospheric regime. (Colour online)

array of thermocouples (16 thermocouples) in the bottom layer ($z = 5$ mm). The temperature difference profiles for numerical simulation and experiment at $z = 5$ mm are shown in figure 13)c. As we can see, the experimental measurements also show a
265 significant temperature increase in the bottom layer without localized central cooling. We also note that the experimental points are closer for the numerical simulation with a large cooler, meaning that the cooling power in the experiment was probably underestimated. Qualitatively, the temperature trends presented are very similar to those obtained by the re-analysis (Screen and Simmonds, 2010).

https://doi.org/10.5194/egusphere-2023-2797
Preprint. Discussion started: 17 January 2024

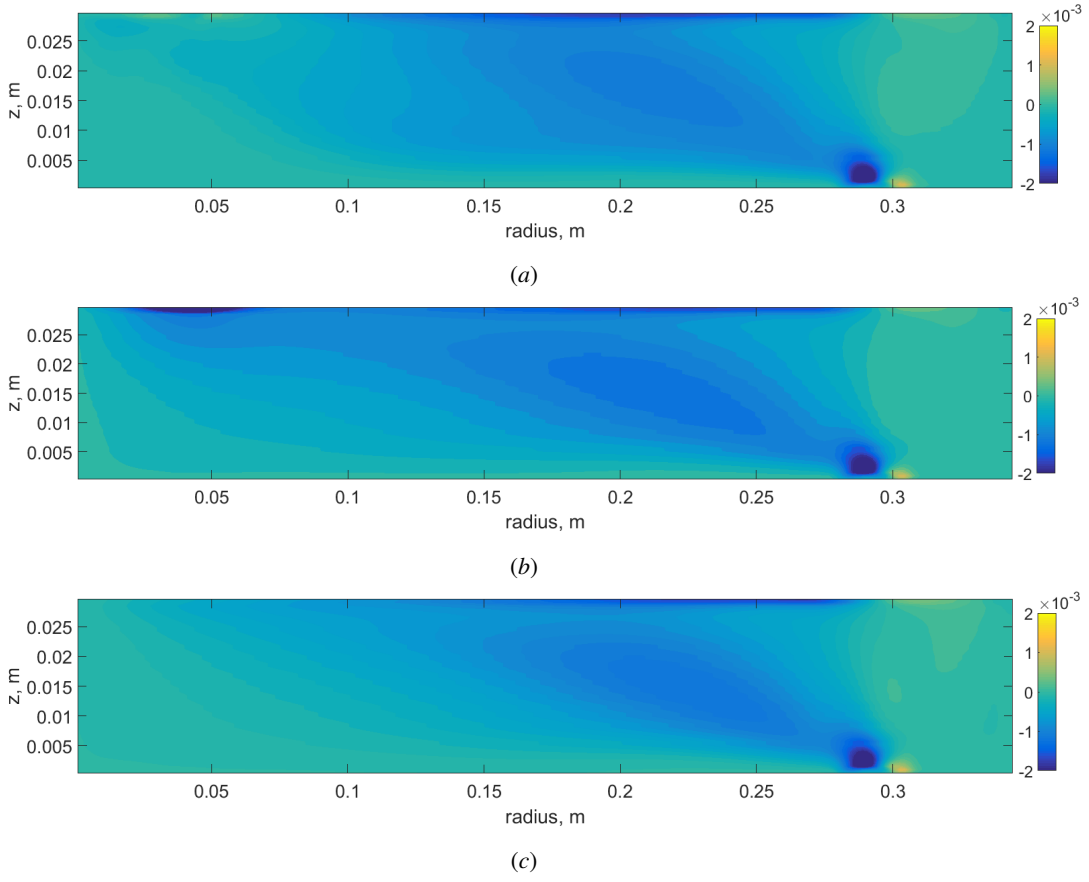

Figure 14. Pulsating part of the radial heat flux $\langle u_r T' \rangle_{\phi,t}$, in $\mathrm{mK/s}$. (a) – regime with large non-slip cooler, (b) – regime with large slip cooler, (c) – regime without cooler. Atmospheric regime. Numerical simulation. (Colour online)

To explain this remarkable transformation of the mean temperature field, it is necessary to analyze the spatial distribution of heat flux. The vertical fields of the pulsating and mean parts of the radial heat flux are shown in figure 14 and figure 15. As we can see the spatial structure of the pulsating part of the heat flux (mainly provided by baroclinic waves) is similar for all cases. The pulsating heat flux transports heat to the upper layer and then to the center. In the lower part of the layer the wave motions are damped by viscous friction and the heat flux near the bottom is mainly provided by the mean circulation (figure 15). The intensive polar cell in the case of a large non-slip cooler provides a cold fluid flux towards the periphery near the bottom (negative heat flux), which cools the lower part of the layer (figure 15a). The transition from non-slip to slip boundary conditions at the localized cooler (switching off the Ekman pumping) leads to remarkable decrease in the negative heat flux near the bottom (figure 15b) and consequently to an increase of the temperature (figure 13). The next transition from the large slip cooler to the uniform cooling results in a further decrease of the negative heat flux (figure 15c). For quantitative comparison of the mean and pulsating heat flux near the bottom, the corresponding profiles are shown in figure 16.

https://doi.org/10.5194/egusphere-2023-2797
Preprint. Discussion started: 17 January 2024

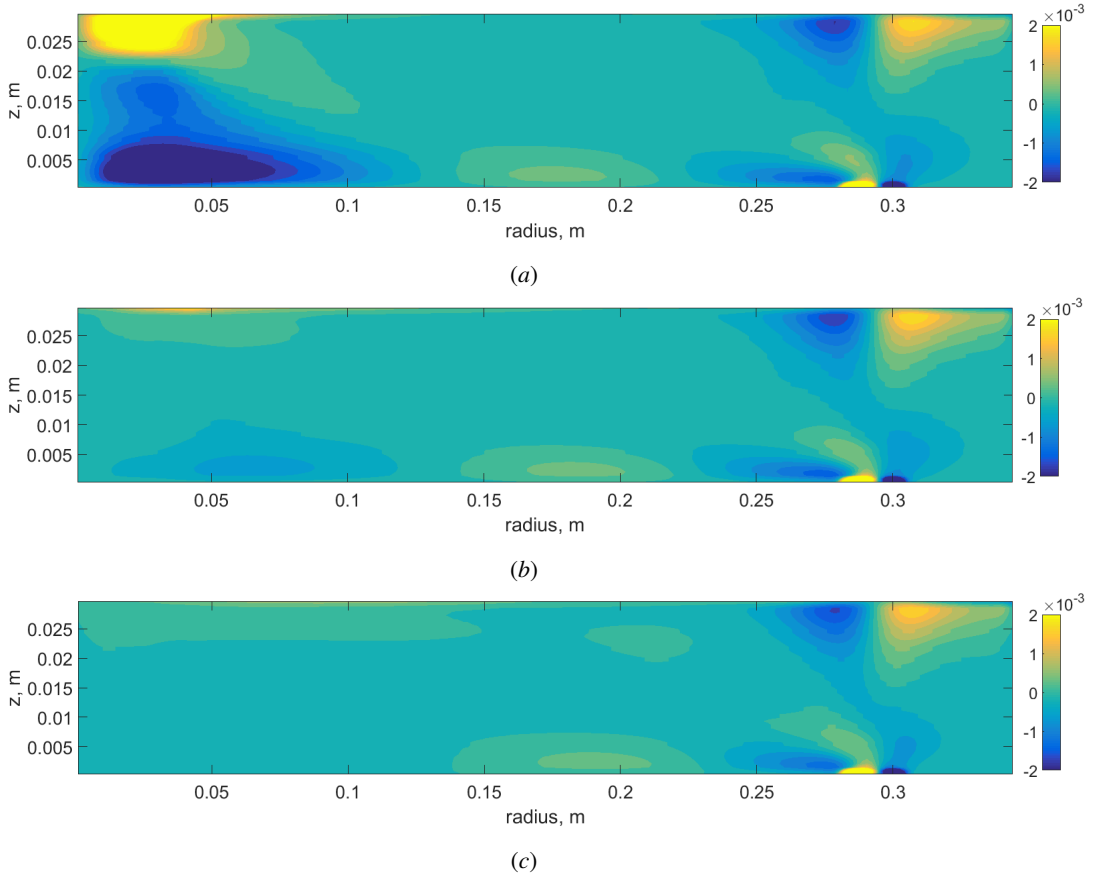

Figure 15. Mean part of the radial heat flux $\langle U_r T \rangle_\phi$, in $\mathrm{mK/s}$. (a) – regime with large non-slip cooler, (b) – regime with large slip cooler, (c) – regime without cooler. Atmospheric regime. Numerical simulation. (Colour online)

5 Conclusions

The results of experimental and numerical modeling of Arctic warming in a laboratory dishpan configuration are presented. Arctic warming is reproduced by varying the size of the local cooler in the "atmospheric" regime, when the structure of the flow is similar to the general atmospheric circulation. Namely, the meridional circulation consists of three cells, laboratory analogs of Hadley cell, Ferrel cell and polar cell. The baroclinic waves in this regime are strongly non-stationary with the main modes $m = 4 - 8$. Numerical simulations show that significant variation of the cooling power and the boundary (slip and non-slip) conditions leads to quantitative changes in the structure and intensity of the baroclinic waves. It is found that deviations of the energy of the main modes for different cases can be up to 25% and the local cooling variation has a strong influence on the structure of the polar cell analog. Special attention is paid to the role of Ekman pumping due to the non-slip condition on the cooler surface. It is found that Ekman pumping results in a strong descending updraft near the axis of rotation, which determines the structure of the central meridional cell. In the case of the slip cooler that better simulates real atmospheric conditions, the

https://doi.org/10.5194/egusphere-2023-2797
Preprint. Discussion started: 17 January 2024

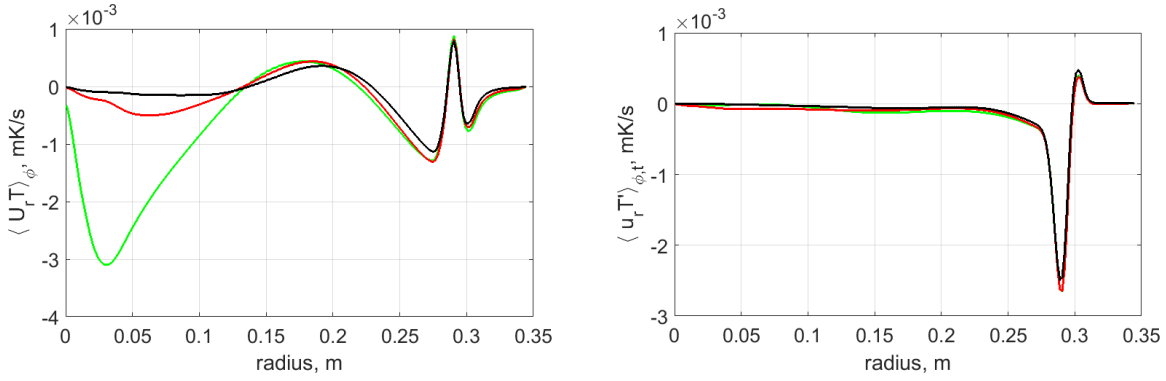

Figure 16. Profiles of the mean and pulsating parts of the radial heat flux near the bottom, at $z = 0.002$ m. (a) – $\langle U_r T \rangle_\phi$; (b) – $\langle u_r T' \rangle_{\phi,t}$. Black line – without cooling, green line – large cooler, non-slip condition, red line – large cooler, slip condition. "Atmospheric" regime. Numerical simulation. (Colour online)

polar cell analog is much weaker and located mainly in the upper layer, closer to the central radii. The transition from the large slip cooler to the uniform cooling ("Arctic warming") results in a weakening of the polar cell analog. The obtained results show that the size and boundary conditions at the cooler surface play a crucial role for the structure and intensity of the polar cell analog.

Another important and widely discussed issue is the change in zonal flow structure and intensity due to Arctic warming. Numerical results show that the transition from large local cooling in the center and uniform cooling over the rest of the free surface to uniform cooling over the whole surface leads to a weakening of the zonal flows.

The main and rather unexpected result of our experimental and numerical of Arctic warming is a noticeable transformation of the mean temperature field, namely, the central region and most part of the lower layer become warmer, while most of the upper layer and the peripheral (equatorial) part of the lower layer become colder. The nature of this phenomenon in the system under consideration is described on the base of our numerical data. It is closely related to the change in the radial heat fluxes. The baroclinic waves transport heat to the upper layer and then to the center. In the lower part of the layer the wave motions are damped by viscous friction and the heat flux near the bottom is mainly provided by the mean circulation. The removal of local cooling leads to a weakening of the analog of polar cell and a significant decrease in the negative heat flux near the bottom, which inevitably leads to an increase in temperature. The results of our modeling cannot be directly extrapolated to the real atmosphere, but the described scenario of a substantial increase in the temperature of the major part of lower layer, provided by transformation of the polar cell structure, can be considered as a plausible explanation for Arctic warming amplification.

Author contributions. All authors contribute equally.

https://doi.org/10.5194/egusphere-2023-2797
Preprint. Discussion started: 17 January 2024

Competing interests. The authors report no conflict of interest.

Acknowledgements. The study was done under the RSF project 22-61-00098.

https://doi.org/10.5194/egusphere-2023-2797
Preprint. Discussion started: 17 January 2024

References

Celik, I. B., Ghia, U., Roache, P. J., and Freitas, C. J.: Procedure for estimation and reporting of uncertainty due to discretization in CFD applications, Journal of fluids Engineering-Transactions of the ASME, 130, 2008.

Evgrafova, A. and Sukhanovskii, A.: Angular momentum transfer in direct numerical simulations of a laboratory model of a tropical cyclone, Geophys. Astrophys. Fluid Dyn., 116, 185–205, 2022.

Francis, J. A. and Vavrus, S. J.: Evidence for a wavier jet stream in response to rapid Arctic warming, Environ. Res. Lett., 10, 014 005, 2015.

Fultz, D., Long, R. R., Owens, G. V., Bohan, W., Kaylor, R., and Weil, J.: Studies of thermal convection in a rotating cylinder with some implications for large-scale atmospheric motions, Springer, 1959.

Harlander, U., Sukhanovskii, A., Abide, S., Borcia, I. D., Popova, E., Rodda, C., Vasiliev, A., and Vincze, M.: New Laboratory Experiments to Study the Large-Scale Circulation and Climate Dynamics, Atmosphere, 14, 836, 2023.

Hide, R.: Some experiments on thermal convection in a rotating liquid, Q. J. Roy. Meteor. Soc., 79, 161–161, 1953.

Lembo, V., Messori, G., Graversen, R., and Lucarini, V.: Spectral decomposition and extremes of atmospheric meridional energy transport in the Northern Hemisphere midlatitudes, Geophysical Research Letters, 46, 7602–7613, 2019.

Lembo, V., Fabiano, F., Galfi, V. M., Graversen, R. G., Messori, G., et al.: Meridional-energy-transport extremes and the general circulation of Northern Hemisphere mid-latitudes: dominant weather regimes and preferred zonal wavenumbers, Weather and Climate Dynamics, 3, 1037–1062, 2022.

Overland, J. E., Dethloff, K., Francis, J. A., Hall, R. J., Hanna, E., Kim, S.-J., Screen, J. A., Shepherd, T. G., and Vihma, T.: Nonlinear response of mid-latitude weather to the changing Arctic, Nat. Clim. Chang., 6, 992–999, 2016.

Read, P. L., Pérez, E. P., Moroz, I. M., and Young, R. M.: General circulation of planetary atmospheres: insights from rotating annulus and related experiments, Modeling Atmospheric and Oceanic Flows: Insights from Laboratory Experiments and Numerical Simulations, pp. 7–44, 2014.

Rodda, C., Harlander, U., and Vincze, M.: Jet stream variability in a polar warming scenario – a laboratory perspective, Weath. Clim. Dyn., 3, 937–950, https://doi.org/10.5194/wcd-3-937-2022, 2022.

Schneider, T.: The general circulation of the atmosphere, Annu. Rev. Earth Planet. Sci., 34, 655–688, 2006.

Scolan, H. and Read, P. L.: A rotating annulus driven by localized convective forcing: a new atmosphere-like experiment, Exp. Fluids, 58, 75, 2017.

Screen, J. A. and Simmonds, I.: The central role of diminishing sea ice in recent Arctic temperature amplification, Nature, 464, 1334–1337, 2010.

Stuecker, M. F., Bitz, C. M., Armour, K. C., Proistosescu, C., Kang, S. M., Xie, S.-P., Kim, D., McGregor, S., Zhang, W., Zhao, S., et al.: Polar amplification dominated by local forcing and feedbacks, Nature Climate Change, 8, 1076–1081, 2018.

Sukhanovskii, A., Popova, E., and Vasiliev, A.: A shallow layer laboratory model of large-scale atmospheric circulation, Geophysical & Astrophysical Fluid Dynamics, pp. 1–22, 2023.

Vasiliev, A., Popova, E., and Sukhanovskii, A.: The flow structure in a laboratory model of general atmosphere circulation, Comput. Contin. Mech., 16, 321–331, 2023.

Wallace, J. M., Deser, C., Smoliak, B. V., and Phillips, A. S.: Attribution of climate change in the presence of internal variability, in: Climate change: multidecadal and beyond, pp. 1–29, World Scientific, 2016.

https://doi.org/10.5194/egusphere-2023-2797
Preprint. Discussion started: 17 January 2024

You, Q., Cai, Z., Pepin, N., Chen, D., Ahrens, B., Jiang, Z., Wu, F., Kang, S., Zhang, R., Wu, T., et al.: Warming amplification over the Arctic Pole and Third Pole: Trends, mechanisms and consequences, Earth Sci Rev ., 217, 103 625, 2021.